Validation and Refinement of a Laminar Neural Mass Model Using in vivo Mice Data

Author: Martina Moreno Fina*
Master en Física dels Sistemes Complexos i Biofísica.
Facultat de Física, Universitat de Barcelona, Martí i Franquès 1, 08028, Barcelona, Spain.†

Advisors: Pau Clusella Coberó[1], Roser Sánchez-Todo[2], and Jordi Soriano Fradera[3,4]
[1]*Department of Medicine and Life Sciences. Universitat Pompeu Fabra, Doctor Aiguader, 88, 08003, Barcelona, Spain.*
[2]*Brain Modeling. Neuroelectrics, Avinguda Tibidabo, 47 bis, 08035, Barcelona, Spain.*
[3]*Departament de Física de la Matèria Condensada.*
Universitat de Barcelona, Carrer de Martí i Franquès, 1, 11, 08028, Barcelona, Spain. and
[4]*Universitat de Barcelona Institute of Complex Systems (UBICS)*
(Dated: June 29, 2023)

Abstract: Gamma oscillations (30-80 Hz) play a crucial role in cognitive functions and are associated with neurological disorders, including Alzheimer's disease. Non-invasive brain stimulation techniques, such as 40 Hz transcranial alternating current stimulation (tACS), offer potential in modulating these oscillations and impact cognitive functions. The complexity of the brain, however, necessitates the use of advanced models for effective understanding and the development of therapies. This study aims to validate a framework combining Neural Mass Models (NMMs) with volume conduction physics that takes into account the brain's physical properties and the distribution of synapses across cortical layers. The validation involves predicting a synaptic distribution across various neuronal groups and employing a Genetic Algorithm (GA) to iteratively refine the model to match experimental data.

Key findings include the ability of the NMM to achieve greater similarity with experimental results by varying stochastic noise and the dominance of gamma and alpha oscillations in experimental data aligning well with model predictions. The GA also shows robustness in fitting the model to experimental data, and the predicted synaptic distribution is evaluated against existing literature for physiological accuracy. Despite limitations, our enhanced NMM provides valuable insights into cortical layer interactions, contributing to the understanding of human brain function and the development of treatments for neurological disorders.

Keywords: Brain Stimulation, Neural Mass Model, Synaptic Distribution, Genetic Algorithm, Neural Oscillations.

I. INTRODUCTION

Gamma oscillations, within the frequency range of approximately 30-80 Hz, have emerged as a pivotal area of study in neuroscience, given their integral role in various cognitive functions, notably memory. These oscillations are associated with several neurological and psychiatric disorders, including Alzheimer's disease [1]. The detection of altered gamma activity in both Alzheimer's patients and animal models highlights the potential for targeted therapeutic interventions [2]. Recently, non-invasive brain stimulation techniques, such as 40 Hz transcranial alternating current stimulation (tACS), have been heralded for their prospective capability to modulate these pivotal gamma oscillations, potentially affecting cognitive functions [3, 4]. tACS administers low-intensity alternating electrical currents to the scalp, with the intent of modulating cortical oscillations [5]. This nascent research domain presents promising opportunities for innovative insights into the treatment of Alzheimer's disease and other related conditions. Despite significant progress in comprehending the neurobiological mechanisms driving these effects, the human brain's inherent complexity underscores the need for continued research utilizing sophisticated and physiologically accurate models to deepen our understanding and facilitate the development of efficient therapies.

Numerous mathematical and computational models have been conceived to explore these intricate brain dynamics more profoundly. The advent of semi-empirical 'lumped' Neural Mass Models (NMMs) in the early 1970s represented a notable leap in this pursuit. Pioneers such as Wilson and Cowan, Freeman, and Lopes da Silva played key roles in constructing this modeling paradigm [6–9]. These models operate based on a systematic process that transforms input neuron firing rates into output firing rates. This is facilitated by synaptic interactions and transfer functions. For instance, the Jansen model, which effectively incorporates these elements and has been widely used, offers a representation of the emergence of alpha brain rhythm [10]. The advancements achieved with these early models have played a pivotal role in paving the way for more sophisticated

* martinamorenofina@gmail.com
† master.complex.biophys@ub.edu

models that more accurately reflect the brain's complexity. One notable development in this field is the laminar model by Neuroelectrics [11], which demonstrates a dominance of gamma and alpha frequencies. However, these models have still limitations and require validation with *in vivo* data. This validation process fine-tunes the model by adjusting parameters, enhancing its accuracy and applicability [11, 12].

While Neural Mass Models (NMMs) do an effective job at encapsulating neural processes within a single-compartment model, they do not completely capture the physical properties observed in experimental data due to the necessity for physical embedding. Sánchez-Todo *et al.*, [11], tackled this issue in the context of the laminar model. Going beyond this, Mercadal *et al.*, [13], made further enhancements by establishing a framework that connects Neural Mass Models with volume conduction physics. This includes the integration of a realistic Finite Element Method (FEM) model, which considers the variation in electrical conductivities of different brain tissues.

In response to current needs in the field, the primary objective of this project is to validate the combination of the NMM presented by Sánchez-Todo *et al.*, [11], together with the enhanced physical framework of Mercadal *et al.*, [13], using *in vivo* mice data.

Our goal is to predict the synaptic distribution among various neuronal groups across cortical layers. In particular, we develop a Genetic Algorithm that iteratively refines the synaptic distribution in the multi-compartmental model in order to maximize the likelihood between the experimental and modeled data sets. In other words, we tune the synaptic distribution until the model's predictions closely match the experimental observations.

In order to validate the results, these predictions are compared with findings that we gathered from an extensive literature review. This step further ensures that the model's output is consistent with established scientific knowledge on synaptic distribution across cortical layers.

This Thesis presents significant advancements in four areas of laminar model validation. First, the adjustment of the model's external input noise critically aligned the model with experimental data. Second, the unmistakable dominance of gamma and alpha oscillations in comparison with other frequencies in the experimental data strengthens the laminar model's predictions, reinforcing its accuracy in mirroring real-world brain dynamics. Third, the success of the Genetic Algorithm in fitting the model to experimental *in vivo* mice data underlines its robustness and adaptability, underscoring the utility of algorithmic approaches in refining and validating complex neuroscientific models. Finally, we compared the fitted model's synaptic distribution with distributions reported in the literature, which promise to improve our understanding of cortical layer interactions.

This Master's Thesis is a part of the Neurotwin project, an innovative initiative funded by the European Union's Horizon 2020 FET Proactive (Grant Agreement 101017716). The objective of Neurotwin is to develop advanced 'Neurotwins,' brain models that can characterize individual pathologies and predict the physiological effects of transcranial electric stimulation. These models are then used to design optimal brain stimulation protocols specifically for Alzheimer's disease. The project involves the deployment of a software platform that integrates mesoscale models to create and personalize the Neurotwins. Once personalized, these models are used to optimize the delivery of electric fields [14, 15].

II. METHODS

A. Data Collection

In this study, we use a Neuropixel probe for data collection. This high-density, multichannel electrode array enables simultaneous recordings of local field potentials (LFP) produced by the collective activity of hundreds to thousands of individual neurons [16] together with the firing rate of individual cells across different depths [17]. For this thesis research, we only worked with LFP data collected. Fig. 1A provides an illustration of the probe, including its dimensions and the number of channels.

The experiment begins with a one-hour recording of spontaneous neural activity to establish baseline data on neuronal firing rates and oscillations along the entire tract where the Neuropixel probe is located. After collecting this baseline data, we apply tACS for 30 minutes at a frequency of 40 Hz and an amplitude of $\pm$ 200 μA. Following the stimulation, another hour of spontaneous neural activity recording takes place to analyze potential changes in neuronal firing rates and oscillations. Fig. 1B outlines the entire protocol. In this study, we center our attention on the pre-stimulation phase, which is essential for understanding the normal functioning of neurons and serves as a reference point to assess the effects of tACS on neural activity.

Brain Stimulation Translational Lab at the University Pablo de Olavide (Seville, Spain) carried out all animal experiments on twelve adult ($3-6$ months old) male C-57J mice (Mus musculus). Before and after surgery, the animals were kept in one room but placed in independent cages. The animals were maintained on a 12-h light/12-h dark cycle with continuously controlled humidity (55 $\pm$ 5 %) and temperature (21 $\pm$ 1 °C). All experimental procedures were carried out in accordance with European Union guidelines (2010/63/EU) and following Spanish regulations (BOE 34/11370-421, 2013) for the use of laboratory animals in chronic experiments. The experiments were also approved by the Ethics Committees of the University Pablo de Olavide and the Neurotwin Consortium. Fig. 1C shows a schematic experimental setup to collect experimental in vivo mice data.

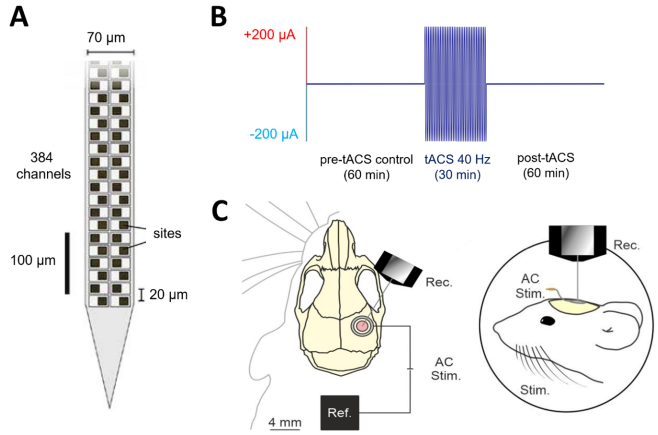

FIG. 1. **A:** Illustration of the Neuropixel probe tip, showing the checkerboard site layout [17]. **B:** Schematic illustration of the protocol used for the data collection [18]. **C:** Schematic illustration of the experimental setup [18].

B. Data Analysis

The local field potential captures the sum of the extracellular electrical potentials generated by the activity of multiple neurons in close proximity to the recording electrode sites on the probe [16]. In the pre-stimulation phase of the experiments, we recorded this spontaneous neural activity using the high-resolution Neuropixel probe [17]. In this project, we focus on the data from a single subject, which had the cleanest recordings. The Dynamical Systems Biology lab at Universitat Pompeu Fabra carried out the data analysis.

The LFP measured by the Neuropixel probe is referenced to a common electrode at the tip of the probe. The first step of data post-processing consists of computing the bipolar LFP (bLFP) by calculating the difference in electrical potentials recorded by two closely spaced electrodes on a single shank of the probe, i.e.:

$$\text{bLPF} = \frac{V_n - V_{n-1}}{h}, \tag{1}$$

where V_n represents the voltage recorded at site n and V_{n-1} denotes the voltage recorded at the previous site, $n-1$. The term $h = 20$ μm is the distance between the two adjacent recording sites.

This technique effectively cancels out common-mode noise and provides better spatial localization, reducing volume conduction effects compared to monopolar LFP recordings [11, 19].

From the 384 recording electrodes of the probe, we only kept those that lay within the mice cortex, as identified by the UPO team, resulting in 136 channel data. From those, we only analyzed the channels of the odd columns of the Neuropixel, as we are interested in the distribution of power across depth. This lead to a total of 64 recording sites.

Then, we divided the time series corresponding to each channel in segments of 10 s. Since the animals could move during the recordings, all the segments containing movement (data provided by the UPO team) were discarded to avoid artifacts, leading to $n = 339$ segments.

For each segment we computed a multitaper power spectra [20], which we denoted as $S_j(\omega)$ with $j = 1, \ldots, n$. The frequency profile above $\Omega = 152$ Hz was discarded since it had little contribution to the total power, and we were interested in frequency ranges below this threshold. The final power profile $\overline{S}(\omega)$ across depths for each subject was given by the average of the n multitaper power spectra:

$$\overline{S}(\omega) = \frac{1}{n}\sum_{j=1}^{n} S_j(\omega).$$

In order to derive the relative power between the alpha, $\overline{S}_\alpha$ and gamma bands, $\overline{S}_\gamma$, we normalized the areas under the curve between the frequency ranges of 4-22 Hz (alpha band) and 32-48 Hz (gamma band) with respect to the total power of the recording. It is worth noting that the $4-22$ Hz frequency range captures more than just the alpha band, yet we labeled it as such due to the peak of the power spectral density appearing at 10 Hz, a frequency characteristic of the alpha rhythm. Likewise, while the gamma band usually extends beyond the 32-48 Hz range, we still referred to this range as the gamma band for simplicity. Thus, we had:

$$\overline{S}_\alpha = \frac{1}{T}\int_4^{22} \overline{S}(\omega)d\omega, \quad \text{and} \quad \overline{S}_\gamma = \frac{1}{T}\int_{32}^{48} S(\omega)d\omega,$$

where

$$T = \int_0^{\Omega} \overline{S}(\omega)d\omega$$

is the estimated total power spectra.

C. Dual-frequency Neural Mass Modeling Framework

Neural Mass Models (NMMs) are mathematical models used to illustrate the collective behavior of neuron populations in specific parts of the brain [21]. A typical modeling approach for NMMs uses second-order differential equations that describe the average post-synaptic potential changes s_m that a neural population m causes to any receiving population.

In order to replicate the dynamics identified in previous experimental research [22], where the amplitude and phase of slow oscillations is observed to modulate fast activity, the team at Neuroelectrics incorporated two well-known Neural Mass Models (NMMs) into the laminar Neural Mass Model (LaNMM), [11]. The first model is the Jansen model [10], which generates slow oscillations

within the alpha frequency range. The second model is a variant of the PING model [23, 24], which produces fast oscillations in the gamma frequency range. It is crucial to note that the laminar model described in Ref. [11] includes not only the Neural Mass Model but also a simple physical embedding. In our study, however, we solely utilized the component of the model that encompasses the NMM.

The Jansen model includes three populations: pyramidal neurons (P1), excitatory cells (SS), and slow inhibitory interneurons (SST). The PING model consists of a pyramidal population (P2) and a fast interneuron population (PV). The diagram in Fig. 2A shows the different neuron groups and their connections. The connections between the models are set up to match experimental findings that show a specific modulation between fast and slow frequencies [11, 22]. This phenomenon is reflected in the model, and illustrated in Fig. 2B and Fig. 2C, respectively.

A simplified formulation of the model from Ref. [11] reads:

$$\begin{aligned}
\ddot{s}_{\mathrm{p1}} &= aA\Phi[c_1 s_{\mathrm{ss}} + c_2 s_{\mathrm{sst}} + c_9 s_{\mathrm{p2}} + s_{\mathrm{ext1}}] - 2a\dot{s}_{\mathrm{p1}} - a^2 s_{\mathrm{p1}} \\
\ddot{s}_{\mathrm{ss}} &= aA\Phi[c_3 s_{\mathrm{p1}}] - 2a\dot{s}_{\mathrm{ss}} - a^2 s_{\mathrm{ss}} \\
\ddot{s}_{\mathrm{sst}} &= bB\Phi[c_4 s_{\mathrm{p1}}] - 2b\dot{s}_{\mathrm{sst}} - b^2 s_{\mathrm{sst}} \\
\ddot{s}_{\mathrm{p2}} &= aA\tilde{\Phi}[c_5 s_{\mathrm{p2}} + c_6 s_{\mathrm{pv}} + c_{10} s_{\mathrm{p1}} + s_{\mathrm{ext2}}] - 2a\dot{s}_{\mathrm{p2}} - a^2 s_{\mathrm{p2}} \\
\ddot{s}_{\mathrm{pv}} &= dD\Phi[c_7 s_{\mathrm{p2}} + c_8 s_{\mathrm{pv}} + c_{11} s_{\mathrm{p1}}] - 2d\dot{s}_{\mathrm{pv}} - d^2 s_{\mathrm{pv}}, \\
\ddot{s}_{\mathrm{ext1}} &= aA(p_1 + \xi_1(t)) - 2a\dot{s}_{\mathrm{ext1}} - a^2 s_{\mathrm{ext1}} \\
\ddot{s}_{\mathrm{ext2}} &= aA(p_2 + \xi_2(t)) - 2a\dot{s}_{\mathrm{ext2}} - a^2 s_{\mathrm{ext2}}
\end{aligned} \tag{2}$$

In this model, we established synaptic connections among populations by three types of synaptic connections:

- Excitatory (AMPA) with PSP amplitude $A = 3.25$ mV and decay rate $a = 100\ \mathrm{s}^{-1}$.
- Slow inhibitiory ($\mathrm{GABA_B}$) with PSP amplitude $B = -22$ mV and decay rate $b = 50\ \mathrm{s}^{-1}$.
- Fast inhibitiory ($\mathrm{GABA_A}$) with PSP amplitude $D = -30$ mV and decay rate $d = 220\ \mathrm{s}^{-1}$.

Here, PSP accounts for post-synaptic potential and refers to the change in membrane potential that occurs after a neuron has received a signal from another neuron across a synapse.

The transfer functions Φ and $\tilde{\Phi}$ transduce the presynaptic population average PSP to the population firing rate. They are taken to be sigmoids, of the form

$$\Phi[s] = \frac{2e_0}{1 + e^{r(v_0 - v)}}, \quad \text{and} \quad \tilde{\Phi}[s] = \frac{2e_0}{1 + e^{r(\tilde{v}_0 - v)}}, \tag{3}$$

where $e_0 = 2.5$ Hz, $v_0 = 6$ mV, $\tilde{v}_0 = 1$ mV, and $r = 0.56\ \mathrm{mV}^{-1}$. The synaptic couplings among populations are given by the vector $c = (c_i) = (108, 33.75, 135, 33.75, 70, 550, 200, 100, 80, 200, 30)$.

Finally, the pyramidal populations P1 and P2 receive an external source of excitatory inputs (ext). These inputs, characterized by noisy PSPs, are driven by an external firing rate centered at each of the pyramidal cells and are subject to pink noise fluctuations, ξ_1 and ξ_2. These pink noise processes are derived by filtering Gaussian noise with a standard deviation of σ.

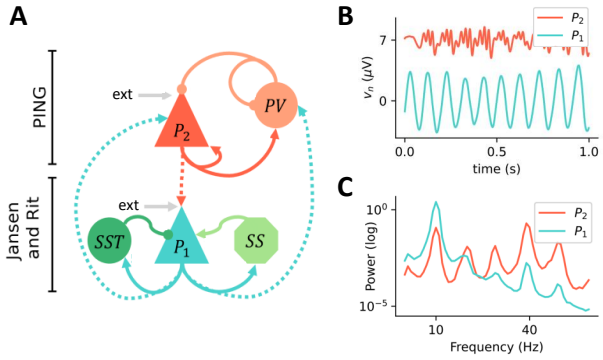

FIG. 2. **A:** Illustration of the neuronal populations and the connectivity between them to match the macaque data in Bastos *et al.*, [22]. Rounded shapes indicate inhibitory populations, while the rest are excitatory. **B:** Membrane potential of the pyramidal populations along time. **C:** Logarithm of the power spectral density of the two pyramidal populations along frequency. Figure adapted with permission from Sánchez-Todo *et al.* from Ref. [11].

D. Physical Model

Our study adopts a physical model approach largely influenced by the work of Mercadal *et al.*, [13]. In their work, they developed an innovative framework for effectively simulating transmembrane currents in pyramidal cells across various cortical layers. This framework ultimately integrates a comprehensive geometrical model with a multi-compartmental neuron model. The primary objective of their work was to create a connection between NMMs and the physical principles responsible for recordings of the brain's electrical activity. As a result of this integration, they were able to simulate SEEG recordings, a technique for invasive brain recordings. These *geometrical* and *multi-compartmental neuron* models are outlined below.

Geometrical Model– The physical model considers the morphology of two single-neuron compartmental models, as depicted in Fig. 3A. Each of these models describes a representative pyramidal neuron from populations P1 and P2 of the NMM presented in [11], which we explained in previous sections. In our study, we assumed that the first pyramidal population extends from layer 1 to layer 5, while the second extends from layer 1 to layer 3.

This Neural Mass Model is incorporated within a layered structure consisting of two isotropic media: gray

matter (GM) and cerebrospinal fluid (CSF). The model estimates synaptic currents, denoted as I_s, by assuming that synapses to pyramidal cells are the primary sources of these currents, as suggested by earlier research [19, 25].

Multi-compartmental neuron model– Then, we use the geometrical model to build a larger model of a cortical region [13]. This model comprises a group of neurons arranged to simulate cortical layers within a geometrically defined volume, as illustrated in Fig. 3B, offering a realistic depiction of cortical activity.

A central aspect of the analysis involves the calculation of the Current Source Density (CSD), denoted as $CSD(z,t)$. The CSD provides a measure of the net volume density of current sources within a small volume of neural tissue at a particular depth z and time t. It is computed as follows:

$$CSD(z,t) = \sum_s \sum_i \nu_{s,i} I_s(z,t) CSD_i(z). \tag{4}$$

In this equation, $\nu_{s,i}$ signifies the probability of a synaptic contact from population s located in layer i. The term $I_s(z,t)$ stands for the synaptic current, which is assumed to be proportional to the post-synaptic potential generated by a synapse in the context of NMM, specifically the laminar model in our study. $CSD_i(z)$ denotes the current source density produced when a unit synaptic current is injected into compartments in layer i of a neuronal population within a cortical patch. Note that the $CSD_i(z)$ values are pre-computed, derived from multi-compartmental, highly detailed geometric models of neurons, as explained in Ref. [13].

Lastly, we used a pre-computed Finite Element Method (FEM) model. This sophisticated technique accounts for the unique electrical conductive properties of different brain tissues and the specific spatial configuration of the Neuropixel probe. By combining the FEM model with the $CSD(z,t)$, it was possible to simulate time-dependent voltages across multiple cortical depths.

The FEM model consists of three layers, representing the white matter (WM), gray matter (GM), and cerebrospinal fluid (CSF). Given the symmetry of the problem, these layers were modeled using an axisymmetric approach. Fig. 3C depicts the geometry of the model and the thicknesses of the layers as well as their conductivity values. We solved for every depth, z, in the CSD distribution, a model with an array of discrete point sources (*i.e.*, line current sources given the model's axisymmetric nature) evenly distributed every 10 μm in the radial direction. A distance of 100 μm was left between the symmetry axis and the nearest source to account for the thickness of the probe and possible infiltration of CSF due to the insertion.

The electric potential distribution was calculated by solving the Laplace equation:

$$\vec{\nabla} \cdot (\beta \vec{\nabla} \lambda) = 0, \tag{5}$$

with additional boundary conditions of the current sources described above and a ground (zero potential) defined along the bounding box. In Eq. (5), β is conductivity and λ is a potential

We extracted the voltage at different depths inside the GM at the symmetric axis and referenced it to a point 10 μm deep in the WM to represent the tip of the probe. Finally, the voltage generated by any distribution $CSD(z,t)$ was calculated by linearly combining it with the solutions of the FEM model.

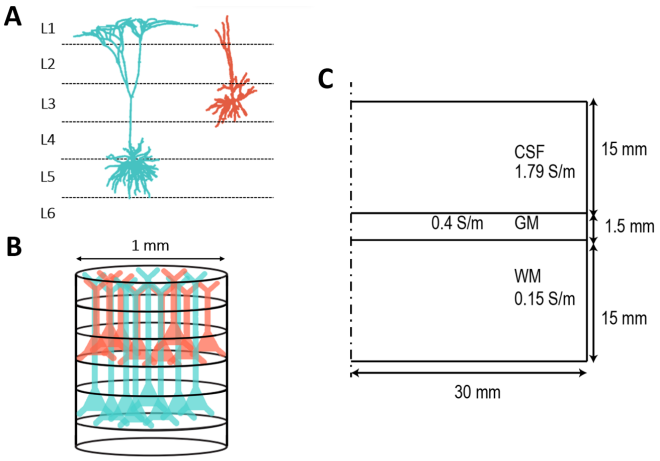

FIG. 3. **A:** Architecture of the laminar model used in our study, consisting of two types of pyramidal cells as described in [11]. In our case, we suppose that the first model spans from layer 1 to layer 5, while the second model spans from layer 1 to layer 3. They are shown with realistic morphology. **B:** The creation process of a multi-compartmental neuron model for the LaNMM. Neurons are spatially distributed within columns in GM, with their somas located inside their corresponding layers. **C:** Schematic representation of the axisymmetric geometry used to simulate a pair of SEEG contacts using the Finite Element Method (FEM).

Clearly, a crucial aspect of the simulation described in Eq. (4) is the synaptic distribution among neuron groups. By altering this synaptic distribution, represented by different $\nu_{s,i}$ values, we could influence the resulting current-source density (CSD) and subsequent voltage. To validate our laminar model, we conducted an extensive analysis of two synaptic distribution tables, one sourced from the literature and another generated by a Genetic Algorithm to best align the model's simulated data with the experimental one.

E. Synaptic Distribution from Literature Review

We created a synaptic probability table, Table I, based on existing literature describing the distribution of synapses between different cells. This table accounts for the spatial distribution of synapses received by the pyramidal cells represented in the P1 and P2 populations of the LaNMM. We have to take into account our

assumption when considering that neurons from the first population span from layer 1 to layer 5, whereas neurons in P2 span from layer 1 to layer 3.

The summary provided in Table I gave insight into the balance between excitation and inhibition in the mammalian cortex and served as a grounded template to generate realistic CSD using the physical model.

To understand the table, it must be noted that pyramidal cells are excitatory neurons found primarily in the cerebral cortex and hippocampus of the mammalian brain. They play a crucial role in cortical connectivity, receiving inputs from various sources, including local inhibitory interneurons, long-range inputs from the thalamus or other cortical areas, as well as other pyramidal cells [26]. In the review that shapes Table I, we considered all the synaptic connections present in the LaNMM. These include glutamatergic coupling from other pyramidal neurons (P1, P2) and excitatory cells (SS).

In the next lines we describe the spatial properties of these different synaptic influences based on existing literature on the distribution of synapses across cortical layers. We also consider the role of GABAergic neurons, which provide inhibitory control and are composed of different subtypes, including parvalbumin (PV) and somatostatin (SST) [27]. Next, we describe the spatial distribution of these synapses based on existing literature.

In layer 1, direct connections between pyramidal cells are rare [28], but we allocate a small proportion of synapses to this layer due to potential connections involving distal tufts of apical dendrites. On the other hand, layers 2 and 3 have strong intralaminar connectivity [29]. However, pyramidal cells in layer 3 have more extensive lateral axonal projections than layer 2 pyramidal cells, which increases the likelihood of synaptic connections in layer 3 compared to layer 2. Finally, we do not allocate any synapse to layers 4, 5, and 6, as we assume that P2 does not extend into these layers.

Almasi *et al.*, [30], discussed the localization of PV+ cells, noting that they are present in all cortical layers except layer 1, with a preference for layers 4 and 5. Their presence in layers 2 and 3 enables them to form synapses with pyramidal cells spanning these layers. The 3/10 proportion in layer 2 and the 7/10 proportion in layer 3 are approximations based on PV+ cells' overall distribution in these layers. Since the pyramidal cell that belongs to the circuit where we model the PV+ population does not extend into layers 4, 5, and 6, it cannot receive synapses from PV+ cells in these layers. Our analysis reflects this by allocating zero proportions to layers 4, 5, and 6.

We simplified SST+ inhibitory neurons to Martinotti cells for our study. These cells contact apical dendrites about half of the time, with the remaining contacts occurring with nearly equal probability at basal dendrites and the tuft, [31]. Mercadal *et al.*, [13], stated that Martinotti cells primarily interact with apical dendrites, which make up roughly half of their connections. Apical dendrites extend across layers 3 and 4, leading to an equal distribution of synapses between these two layers, with 1/4 of the connections in layer 3 and another 1/4 in layer 4. The remaining half of the connections are split almost evenly between basal dendrites and the tuft, resulting in 1/4 of the connections occurring at the tuft and another 1/4 involving basal dendrites. Since tuft inputs are equally distributed between layer 1 and layer [32], the synapses directed to layer 1 result in 1/8 and 1/8 to layer 2. Similarly, basal inputs are distributed, allocating 1/8 of synapses to layer 5 and 1/8 to layer 6. In our case, however, the pyramidal cell considered does not extend to layer 6. Hence, the basal inputs are solely directed to layer 5. This adjustment increases the percentage of synapses in layer 5 to 1/4, while layer 6 does not receive any connections.

External inputs, primarily associated to signals from the thalamus and other cortical regions, also play an important role in neuronal communication. Most notably, these thalamic and higher-order cortical inputs target the upper layers and, to a lesser degree, layer 5 [13, 31]. To reflect this pattern, we distributed the synapses of the first pyramidal cell, which extends from layer 1 to layer 5, as follows: 2/5 of the synapses are allocated to each of layers 1 and 2, with the remaining 1/5 directed to layer 5. For the second pyramidal cell, which is limited to layers 1 through 3, the synaptic distribution is different. We assigned half of the synapses to each of layers 1 and 2. This distribution acknowledges the cell's extension limitations and reflects the concentrated external inputs in the upper layers.

Lastly, the excitatory input labeled 'SS' primarily originates from other pyramidal cells [13]. These connections predominantly take place at the basal dendrites in layer 5 (2/3 of the time), while less frequently, they occur at the apical dendrites (1/3 of the time) [32]. In accordance with these findings, our table shows no connections in layers 1 and 2, a 1/6 connection probability in layer 3 and layer 4, and a peak of 2/3 in layer 5.

TABLE I. Heatmap table representation of the synaptic distribution in the cortex of the populations considered in the laminar model based on the literature review. Each row corresponds to a particular synaptic connection, denoted as 'source→target'. The columns L1 to L6 represent the six different layers of the cortex. Each cell indicates the probability of the respective connection in the respective cortical layer. The color intensity in each cell represents the magnitude of the probability, with darker blue indicating a higher probability.

	L1	L2	L3	L4	L5	L6
ext->P1	2/5	2/5	0	0	1/5	0
SS->P1	0	0	1/6	1/6	2/3	0
SST->P1	1/8	1/8	1/4	1/4	1/4	0
P2->P1	1/7	2/7	4/7	0	0	0
P2->P2	1/7	2/7	4/7	0	0	0
PV->P2	0	3/10	7/10	0	0	0
ext->P2	1/2	1/2	0	0	0	0
P1->P2	1/7	2/7	4/7	0	0	0

F. Genetic Algorithm

A Genetic Algorithm (GA) is a heuristic search that simulates the process of natural evolution, employing mechanisms inspired by biological genetics such as selection, crossover (recombination), and mutation. These evolutionary strategies guide a population of potential solutions towards an optimal one, with the quality of each solution evaluated by a defined fitness function. Over successive generations, the population converges toward the best solution for a given problem [33].

In our work, every stage of the Genetic Algorithm, from the initial design to final execution and performance evaluation, was developed and handled solely by the author. Additionally, a simplified pseudocode of the Genetic Algorithm is available in the appendix under *Pseudocode of Genetic Algorithm.*

Our task is to find a synaptic distribution table, which in this case is represented as a matrix, that makes the model best fit the experimental data obtained from a Neuropixel probe. A population, P, of candidate matrices, which detail connections among various neuron groups across different layers, serves as the chromosomes in our Genetic Algorithm (GA). These matrices evolve towards an optimal solution.Below we outline the most important processes of the algorithm.

Initialization– The Genetic Algorithm starts with the creation of an initial population of chromosomes $c \in P$, where each chromosome $c = (c_{ij})$ is a potential solution represented as a 8×6 matrix. Each row of the matrix represents the different cortex layers, from 1 to 6, while the columns signify synapses between two different groups of neurons.

We generate the initial P randomly. Elements in the synaptic distribution matrix are initialized with random values between 0 and 1, while considering the physical structure of the model. Certain elements are set to zero due to physiological constraints. Specifically, connections to layers $4-6$ from the second pyramidal cell, which are not physically possible as this cell spans layers 1 to 3 and, similarly, connections to layer 6 in the first pyramidal cell.

In addition, each row of the matrix must sum up to 1 as it represents 100% of the synapses across a specific layer ($\sum_{j=1}^{6} c_{ij} = 1, \quad i = 1, \ldots, 8$). Hence, after filling all elements, each row is normalized to preserve the interpretation of these values as probabilities.

Fitness function– The algorithm's goal is to maximize the similarity in the relative powers of the alpha ($4-22$ Hz) and low gamma ($32-48$ Hz) frequency bands across depths between the model output and the experimental data. Relative power is computed as the ratio of power within a specified frequency band to the total power across all frequencies at each depth, providing an index of the dominance of these rhythms in the signal generated by the model.

In order to calculate these relative powers, we use a laminar Neural Mass Model embedded within a multicompartmental neural model. This model takes the synaptic distribution (c in the Genetic Algorithm) as input and produces a simulated Neuropixel-like voltage signal, which reflects the electrical activity within the brain.

From this voltage signal, we compute the bipolar local field potential (bLFP) by taking the difference between consecutive voltage values. Using Welch's method, we then quantify the power spectral density ($\overline{S}$) of this bLFP. This method divides the data into overlapping segments, computes a periodogram for each segment by applying a window function, and averages these periodograms to obtain $\overline{S}$, which details the power of the signal across different frequencies.

Finally, we derive the relative power for each depth within the alpha and gamma frequency bands from the $\overline{S}$. For each depth and specified frequency band, we sum the power within the band and divide it by the total power across all frequencies at that depth. This is done for both the $4-22$ Hz (alpha band) and $32-48$ Hz (gamma band), providing an indication of the dominance of each rhythm (alpha and gamma) in the signal generated by the model at each depth.

Before evaluating fitness, we ensure that the model-generated and experimental data are comparable. To accomplish this, we interpolate the experimental data to match the model's higher spatial resolution, aligning the structure of the experimental data with that of the model.

We do the evaluation of the similarity between the two data sets by computing the Pearson correlation coefficients separately for alpha and gamma bands, ρ_α and ρ_γ, as:

$$\rho_\alpha(c) = \frac{\mathrm{cov}(\overline{S}_\alpha^{exp}, \overline{S}_\alpha(c))}{\sigma(\overline{S}_\alpha^{exp})\, \sigma(\overline{S}_\alpha(c))}, \tag{6}$$

$$\rho_\gamma(c) = \frac{\mathrm{cov}(\overline{S}_\gamma^{(exp)}, \overline{S}_\gamma(c))}{\sigma(\overline{S}_\gamma^{exp})\, \sigma(\overline{S}_\gamma(c))}, \tag{7}$$

where $\overline{S}_\alpha^{exp}$ is the relative power within the alpha frequency given the experimental data and similarly $\overline{S}_\gamma^{exp}$ for the gamma band. On the other hand, $\overline{S}_\alpha(c)$ and $\overline{S}_\gamma(c)$ are the simulated relative powers data for a chromosome, c, in the alpha and gamma frequency bands, respectively.

The coefficients ρ_α and ρ_γ measure the correlation between the model-generated and experiment-derived relative powers across depths. Subsequently, we take the average of these two Pearson correlation coefficients, $\rho(c) = (1/2)(\rho_\alpha(c) + \rho_\gamma(c))$. A high average correlation coefficient suggests that the relative powers produced by the model closely align with those from the interpolated experimental data.

Selection– The selection process in the Genetic Algorithm aims to identify the fittest chromosomes in

P to produce new offspring. This process relies on evaluating the performance of each individual, with those demonstrating better performance, as indicated by a higher Pearson correlation coefficient, being assigned a greater probability of being chosen as parents for producing new offspring. Consequently, this selection process promotes the propagation of favorable traits and enhances the overall quality of P by favoring individuals with superior performance.

Crossover– After the selection process, pairs of parents undergo the crossover operation to produce offspring, constituting the new P. The occurrence of this operation is determined by the crossover rate, r_c, which controls the extent of genetic recombination. In our approach, we utilize an interpolation-based recombination process applied independently to each row. Rather than directly mixing the parents, we assign random weights, W, to each parent during offspring creation, allowing for a more intricate exploration of the solution space and promoting genetic diversity. Subsequently, to maintain the coherence and validity of the synaptic matrix, we normalize each row to ensure that the probabilities sum up to 1.

Mutation– The subsequent step involves applying a mutation operation to the offspring. Mutation is a vital mechanism for maintaining genetic diversity within the P and avoiding premature convergence to suboptimal solutions. During mutation, a random element in the c matrix, except for those previously restricted to 0, is selected and altered by assigning it a new value between 0 and 1. The probability of this process occurring is determined by the predefined mutation rate, r_m, that governs the extent of genetic mutation. To ensure the integrity of the synaptic matrix and preserve its meaningful interpretation, a normalization is performed on the modified row, ensuring that the probabilities continue to sum up to one.

Solution Evolution– The Genetic Algorithm progresses through multiple generations, evolving its P with each iteration. In each generation, c undergoes selection, crossover, and mutation operations, collaborating to produce increasingly superior solutions.

After completing the specified number of generations, N_{gen}, the GA determines the best solution obtained during the evolutionary process. This solution represents the synaptic distribution matrix that maximizes the similarity between the relative powers across depth for the alpha and gamma frequency bands computed from modeled and experimental data. The determination of the best solution is based on the highest fitness value.

Through this iterative process, the genetic algorithm explores a diverse range of potential solutions, gradually refining the synaptic distribution matrix to closely match the output of the model with the experimental data.

1. *Genetic Algorithm Parameters*

The Genetic Algorithm adopted in our research operates based on four crucial parameters, as outlined in Table II. These parameters are fine-tuned through manual adjustment following careful observation of the algorithm's behavior under varying parameter values.

- Population size, P_{size}: Total number of chromosomes present in each generation.
- Number of generations, N_{gen}: Count of iterative cycles the algorithm goes through.
- Mutation rate, r_m: Likelihood of chromosomes undergoing spontaneous alterations or 'mutations'.
- Crossover rate, r_c: Probability of chromosomes to intermix in order to create offspring.

TABLE II. Values of the parameters used in the Genetic Algorithm

Parameter	**Value**
Population Size, P_{size}	10
Number of generations, N_{gen}	10^5
Mutation Rate, r_m	0.40
Crossover Rate, r_c	0.75

In our research, we employed a Genetic Algorithm to tackle a complex problem while managing computational resources effectively. Due to the high computational cost per individual evaluation in our problem, we opted for a smaller population size of 10. This choice ensured manageable computation at each generation.

However, to ensure a broad exploration of the solution space over time, we offset the smaller P with a large $N_{gen} = 10^5$ in this case. This high number of generations allowed for extensive search space exploration, providing more opportunities for genetic operations like crossover and mutation.

In essence, our strategy navigates the trade-off between computational feasibility and solution quality by adjusting P_{size} and N_{gen}. This approach maintains reasonable computational costs while effectively exploring diverse solutions, a critical aspect in the application of Genetic Algorithms to complex problems.

Regarding the r_m, we inform our selection by preliminary simulations spanning 5000 generations. During these simulations, we vary the mutation rates within the range of 0.1 to 0.4, while keeping the crossover rate constant at 0.9. We decided to maintain this particular r_c during our exploratory study because of its typical effectiveness in Genetic Algorithms [34]. However, any value can be selected as our key interest is observe the interplay between the mutation rate and fitness.

We strategically selected the range for r_m. The lower limit of 0.1, which is conventionally considered high for

many problems, was established to promote genetic diversity and mitigate the risk of converging prematurely to local minima, a common challenge in our problem given the presence of excitatory, inhibitory, and noise contributions. We chose an upper limit of 0.4 to ensure that less than 50% of an offspring's genes are likely to mutate. This limit is important to prevent the Genetic Algorithm from acting as a purely random search, thus maintaining the significance of offspring generated through the crossover. With an excessively high r_m, beneficial combinations of genes that could lead to improved solutions might be altered too frequently, thereby diminishing the effectiveness of the crossover operation.

As shown in Fig 4 (top), a mutation rate of 0.4 optimally enhances the performance of our Genetic Algorithm. Although this rate might be considered high compared to traditional standards [34], it favorably promotes population diversity and guards against premature convergence to sub-optimal solutions.

In regards to the crossover rate, we decided to set it to 0.75 based on the evidence presented in Fig 4 (bottom). This chart shows that a r_c of 0.75 results in the highest fitness during relatively short simulations of 5000 generations, with r_m held constant at 0.4, a value selected based on its superior performance in Fig 4 (top).

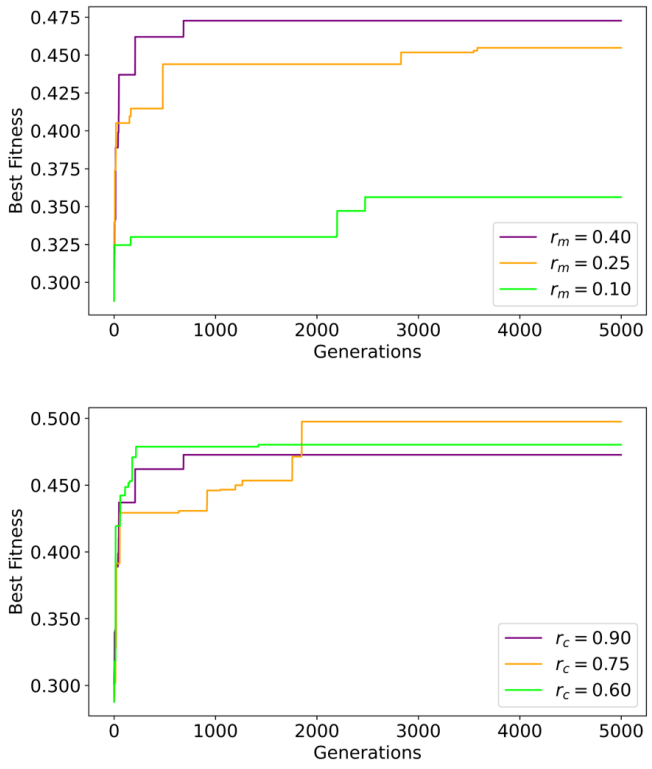

FIG. 4. Evolution of optimal fitness given varying parameters. **Top**: Comparison among different mutation rates, r_m, with a constant crossover rate of 0.90. **Bottom**: Comparison among different crossover rates, r_c, with a constant mutation rate of 0.40.

In our exploration, we considered three different crossover rates, spanning a range from 0.6 to 0.9. The decision to restrict our scope within this range is twofold. Firstly, we aim to ensure that, with a probability greater than half, a new offspring would be created by merging the solutions of two parents, thereby fostering solution diversity and effective exploration of the problem space. This idea informs our decision for a lower limit of 0.6. On the other hand, we set the upper limit to 0.9 to avoid an excessively high rate of crossover that might lead to new offspring being almost always generated through crossover. Such a scenario could potentially limit the variability within the population and hinder the exploration of new solution spaces [34].

Our findings show that a balance between these two extremes, represented by a r_c of 0.75, provides the most effective approach in our case, enabling the Genetic Algorithm to robustly search the problem space while simultaneously refining promising solutions.

The simulation time for our study, employing the parameters shown in Table II, is approximately 57 hours. This computation was conducted on a high-performance computer at Neuroelectrics enterprise equipped with 120 cores. To leverage this computational power and expedite the simulation process for each individual, we implemented a multi-threading approach. This strategy allowed us to concurrently generate data for each chromosome across all generations, substantially reducing the overall computation time. Consequently, we managed to perform a detailed exploration of the solution space with a large N_{gen} within a practical time frame.

III. RESULTS

A. Fitting the Model's Stochastic Noise to Experimental Data

The primary goal of the initial phase of our research is to tailor the stochastic external input to more closely resemble experimental data. This noise is represented as pink noise, denoted as `ext` in Fig. 2A, with each pyramidal cell being assigned its unique noise value.

Pink noise, also known as 1/f noise, is a signal or process characterized by a frequency spectrum wherein the power spectral density inversely correlates with the frequency. Within our model's framework, pink noise symbolizes external inputs primarily arising from the thalamus and other cortical regions.

We preserve the mean value of this pink noise at the levels set in the foundational laminar model study, which is 200 Hz for P1 and 90 Hz for P2 [11]. By doing so, we safeguard the integrity of the external input's power and frequency domain characteristics since any alteration to these mean values can potentially distort the natural population dynamics.

On the other hand, to achieve better alignment with the experimental data, we adjust the standard deviation (σ). The laminar model initially set σ at a constant 5 Hz.

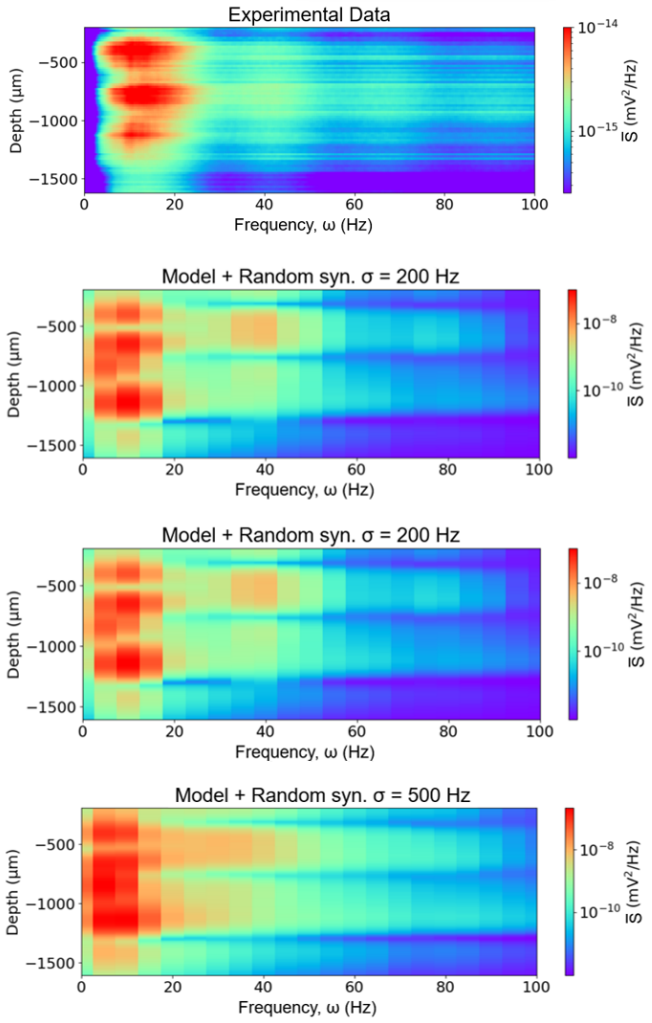

FIG. 5. **Comparative Power Spectral Density Analysis for Experimental and Model-Simulated Data under Different Noise Conditions**: This panel illustrates four color-coded logarithmic scale plots of power spectral density, $\overline{S}$, measured in $\mathrm{mV}^2/\mathrm{Hz}$. The range extends from frequencies of 0 Hz to 100 Hz and depths from -200 μm to -1600 μm, with warmer colors signifying higher $\overline{S}$ values. The top plot showcases the $\overline{S}$ derived from experimental data while the others represent the $\overline{S}$ of model-simulated data using a random synaptic distribution with different selected standard deviations (σ = 200 Hz, 50 Hz, 500 Hz).

However, our research finds that an increase in this value leads to a more accurate replication of the experimental data by visual inspection. As evident in Fig. 5, a σ of 200 Hz yields a heat map most resembling that of the experimental data, whereas 50 Hz was deficient, and 500 Hz was excessively high.

This qualitative strategic adjustment of the standard deviation for our external input noise allowed us to enhance the model's precision, thereby achieving a more accurate depiction of the neuronal behavior observed in our experimental data.

B. Dominance of Gamma and Alpha Oscillations

One of the central aspects of this study relates to the dominance of gamma and alpha oscillations in comparison with other frequencies predicted by the laminar model [11]. This dominance emerges from our dual-frequency approach of the laminar model [11]. This characteristic has been previously demonstrated in Fig. 2, which represents the logarithm of the power spectral density across frequencies for the two pyramidal populations.

In Fig. 6A, we see the congruity between the experimental and model-simulated data, represented by the mean power spectral density across depth. The shaded areas, corresponding to the alpha ($4 - 22$ Hz) and low gamma ($32 - 48$ Hz) frequency bands, align with the peaks of the mean $\overline{S}$. This agreement underscores the dominant oscillatory activities within these frequency bands in the experimental data, thereby affirming the validity of our combined model. Notably, this correspondence holds even when the simulated data is obtained using a random distribution of synapses, reflecting the inherent nature of the dual-frequency approach within the model.

However, a discrepancy arises when examining the relative power distribution across cortical depth, as shown in Fig. 6B. Despite adhering to the dual-frequency approach, the model-simulated data, under the assumption of a random synaptic distribution, diverges noticeably from the experimental data, especially within the gamma frequency band. This deviation emphasizes the pivotal role that the realistic physical layer [13] plays in shaping the relative power across different cortical layers. It points to the need for refining our model with a more informed synaptic distribution to accurately emulate the experimental observations.

C. Model Fitting with Genetic Algorithm

The third part of our study focuses on refining our model for a more accurate alignment with experimental observations in the relative power profiles. To this end, we employ a Genetic Algorithm (GA) to identify the synaptic distribution that most accurately matches the experimental data.

Fig. 7 A illustrates the effectiveness of the GA, charting the progression of the best fitness scores over generations, computed separately for both alpha and gamma, as well as the total best fitness. We calculate the total best fitness as the average of Pearson's correlation values for the alpha and gamma of each chromosome. Thus, the depicted best fitness in the plot is not a straightforward mean of the individual best fitness scores shown since the best fitness for alpha may be achieved by a different chromosome than the one achieving the best gamma fitness.

The best fitness values shown represent the highest Pearson coefficients identified across all prior generations,

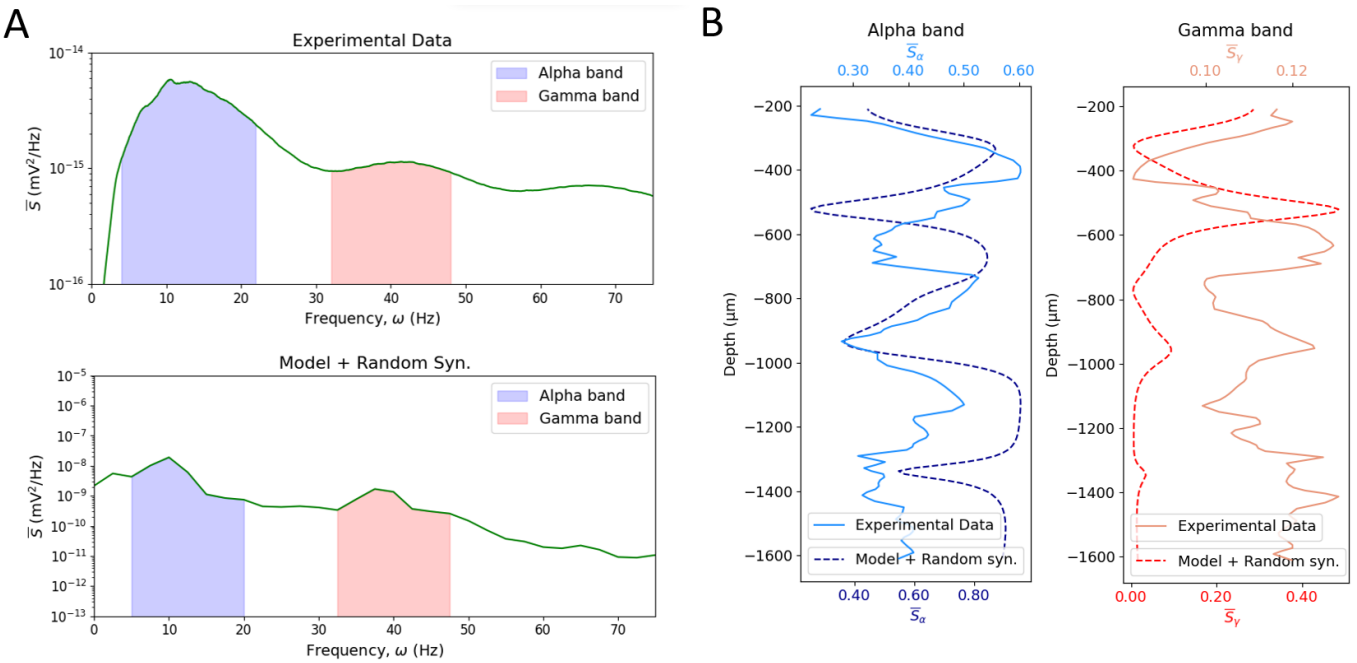

FIG. 6. **A: Mean Power Spectral Density Comparison**: The top graph here represents the mean $\overline{S}$ for experimental data, and the bottom graph illustrates the mean $\overline{S}$ for model-simulated data with a random synaptic distribution. The mean $\overline{S}$ (green line) is calculated across all depth points for each frequency in the 0-75 Hz range. The alpha (4-22 Hz, shaded in blue) and gamma (32-48 Hz, shaded in red) frequency bands are highlighted. $\overline{S}$ values are presented on a logarithmic scale for improved visualization. **B: Relative Power of Cortical Activity Across Cortical Depth Comparison**: This panel compares the relative power of cortical activity across cortical depth between experimental data (continuous, lighter lines) and model-simulated data with a random synaptic distribution (marked by dashed, darker lines). The relative power is plotted against cortical depth, represented in μm. The plot on the left shows the relative power of the alpha frequency band (blue), and the plot on the right illustrates the relative power of the gamma band (red).

updated only when a superior value is discovered. This progression indicates that, as the generations evolve, the model-simulated data increasingly aligns with the experimental data, resulting in progressively higher Pearson coefficients.

This trend clearly illustrates the evolutionary nature of synaptic distribution, exploring a broad array of potential solutions and selecting the most suitable ones for further evolution. This evolution occasionally stalls due to numerous local minima introduced by the interplay of excitatory, inhibitory processes and noise. However, these stalls are counteracted by a high r_m, set as a model parameter. The process culminates in achieving a Pearson coefficient of 0.67, marking it as the best total fitness.

Fig. 7B visually depicts the synaptic distribution predicted by the Genetic Algorithm (GA). A more intense blue color represents a higher connection probability, providing an in-depth view of the synaptic distribution across the various cortical layers. It is important to note that the zeros appearing in layer 6, and in layers 4 and 5 for the second pyramidal cell, are predetermined. This consideration aligns with our initial supposition that the first pyramidal cell extends from layer 1 to layer 5, while the second one extends from layer 1 to layer 3.

Finally, Fig. 7C illustrates the relative powers of the alpha and gamma frequency bands across depth. When comparing these plots to those depicted in Fig. 6B, we notice a closer resemblance between the model's data and experimental data when using the synaptic distribution optimized by the GA. This observation confirms the effective role of the GA in refining the model to more accurately emulate the experimental data, further emphasizing the vital role of synaptic distribution within our model.

D. Comparison between the Distribution of Synapses Predicted with GA and Literature

In Fig. 8A, we can observe the quadratic interpolation of synaptic distribution across six cortical layers (L1-L6) for eight distinct synaptic connections, categorized based on the two types of pyramidal cells. The synapses' origins are color-coded as per the legend on the left, which corresponds to the color scheme presented in Fig. 2A.

We show the synaptic distribution for three scenarios: one based on literature data, another predicted by the Genetic Algorithm (GA), and a third one following a random distribution. Each of them presents distinct patterns and characteristics that are worth noting.

A

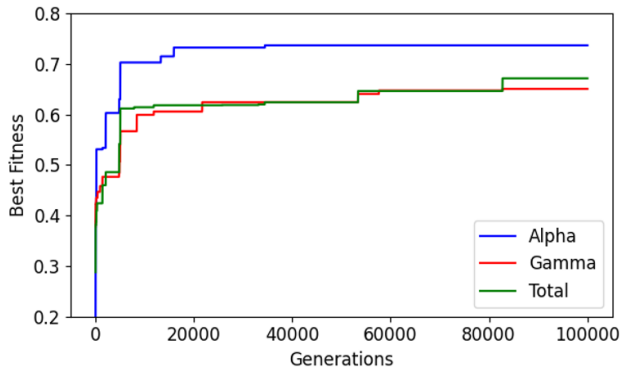

B

	L1	L2	L3	L4	L5	L6
ext->P1	0.08	0.21	0.12	0.11	0.48	0.0
SS->P1	0.09	0.27	0.23	0.24	0.18	0.0
SST->P1	0.18	0.18	0.02	0.05	0.56	0.0
P2->P1	0.42	0.38	0.21	0.0	0.0	0.0
P2->P2	0.36	0.3	0.34	0.0	0.0	0.0
PV->P2	0.5	0.37	0.13	0.0	0.0	0.0
ext->P2	0.32	0.36	0.32	0.0	0.0	0.0
P1->P2	0.13	0.69	0.18	0.0	0.0	0.0

C

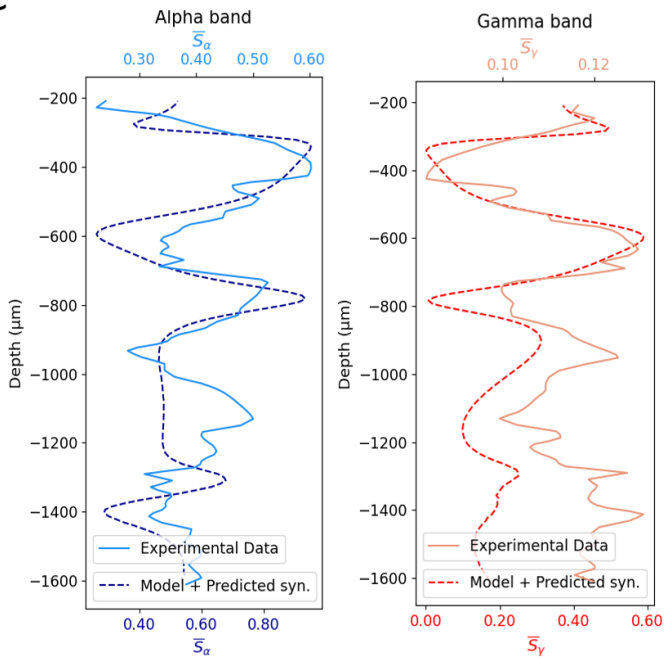

FIG. 7. **A: Evolution of Fitness Scores in Genetic Algorithm**: Illustration of the evolution of the best fitness scores over successive generations of the Genetic Algorithm. The total fitness score (green) represents the average of the Pearson correlation coefficients for the alpha and gamma frequency bands, thus demonstrating the convergence of the model over time. The individual evolutions of the best fitness scores for the alpha (blue) and gamma (red) frequency bands are also displayed. **B: Heatmap Table of Synaptic Distribution Predicted by Genetic Algorithm**: A heatmap table representation of the synaptic connection probabilities in the cortex of the populations considered in the laminar model, as predicted by the Genetic Algorithm. Each row corresponds to a specific synaptic connection, denoted as 'source→target'. The columns L1 to L6 represent the six different layers of the cortex. Each cell illustrates the probability of the respective connection in the corresponding cortical layer. The color intensity in each cell symbolizes the magnitude of the probability, with a darker shade of blue signifying a higher probability. **C: Comparison of Relative Power of Cortical Activity across Cortical Depth**: This section compares the relative power of cortical activity across cortical depth between experimental data (continuous, lighter lines) and model-simulated data using the synaptic distribution predicted by the Genetic Algorithm (dashed, darker lines). The relative power is plotted against cortical depth in μm. The plots display the relative powers for the alpha (blue, on the left) and gamma (red, on the right) frequency bands, thus providing insights into the model's performance at different frequency ranges.

Upon a preliminary inspection, The plot reveals clear differences in the synaptic distribution profiles across different layers of the cortex. The random distribution exhibits sharp fluctuations between layers, suggesting a lack of smooth transitions that might not reflect biological reality. In comparison, the GA-predicted distribution portrays a smoother transition, suggesting a more consistent representation of synaptic connections within the cortex. Lastly, the literature-based distribution seems to be intermediate, presenting some variability across layers while retaining an element of smoothness present in the GA-predicted distribution.

Fig. 8B presents two tables that outline the discrepancies between the synaptic distribution derived from literature and two distinct methodologies: a random distribution and a GA prediction incorporated within a physically embedded laminar model in a multi-compartmental neural model. These tables utilize higher and lower values to indicate larger and smaller deviations from the literature data, respectively.

An initial observation when scrutinizing these tables is the notable discrepancy in the 'ext→P2' connection under the random distribution, where the differences reach a value of 0.90. In contrast, the GA prediction considerably mitigates this discrepancy for the 'ext→P2' connection, resulting in values from 0.18 to 0.32.

The highest discrepancy observed for the GA-predicted synapses is markedly lower than the one seen in the random predictions (0.57 vs. 0.90), thereby reinforcing the relative superiority of the GA predictions.

However, it is crucial to note that the GA predictions do not exhibit uniform superiority across all connections. For instance, the 'PV→P2' connection illuminates a potential shortfall of this distribution. Particularly in layer 1, the predictions for this connection demonstrate a more significant deviation from the literature data compared to the random distribution.

A

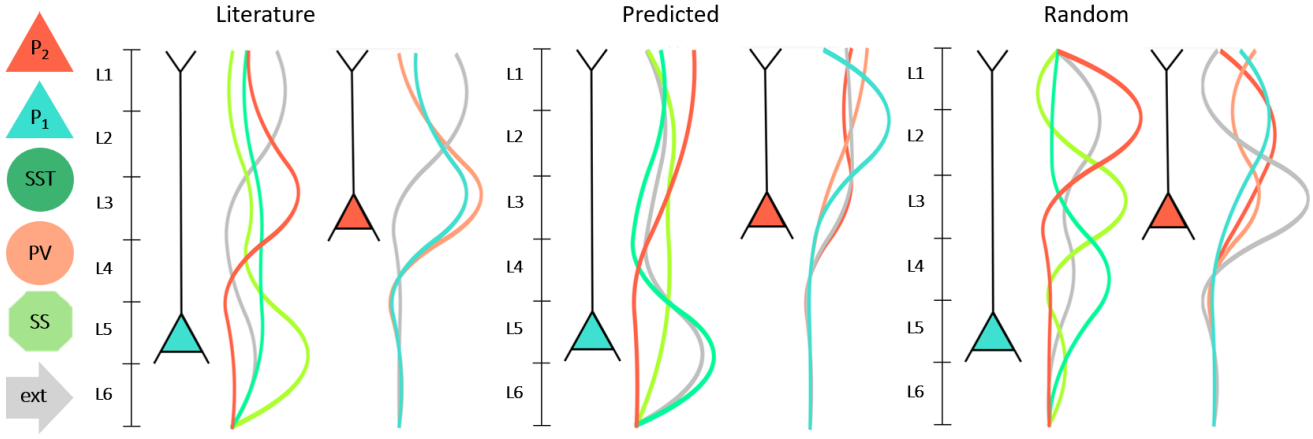

B

Literature - Predicted

	L1	L2	L3	L4	L5	L6
ext->P1	0.32	0.19	0.12	0.11	0.28	0.00
SS->P1	0.09	0.27	0.06	0.07	0.49	0.00
SST->P1	0.06	0.06	0.23	0.20	0.31	0.00
P2->P1	0.27	0.09	0.36	0.00	0.00	0.00
P2->P2	0.22	0.01	0.23	0.00	0.00	0.00
PV->P2	0.50	0.07	0.57	0.00	0.00	0.00
ext->P2	0.18	0.14	0.32	0.00	0.00	0.00
P1->P2	0.02	0.41	0.39	0.00	0.00	0.00

Literature - Random

	L1	L2	L3	L4	L5	L6
ext->P1	0.32	0.08	0.16	0.23	0.15	0.00
SS->P1	0.07	0.01	0.56	0.12	0.52	0.00
SST->P1	0.04	0.10	0.13	0.32	0.05	0.00
P2->P1	0.05	0.57	0.53	0.00	0.00	0.00
P2->P2	0.07	0.29	0.22	0.00	0.00	0.00
PV->P2	0.38	0.11	0.27	0.00	0.00	0.00
ext->P2	0.48	0.42	0.90	0.00	0.00	0.00
P1->P2	0.12	0.24	0.36	0.00	0.00	0.00

FIG. 8. **A**: **Quadratic Interpolation of Synaptic Distributions**: This figure shows the quadratic interpolation of synaptic distributions based on literature (left), predicted by the GA (middle), and of a random distribution (right). The interpolated probability distributions are plotted across six layers (L1-L6) of the cortex for eight distinct synaptic connections, as described in the laminar model. The interpolation was performed using a quadratic function to ensure a smoother representation of the distribution. The connections are divided into two groups, each representing a different type of pyramidal cell. The color legend on the left indicates the source of the synapses and corresponds to the color code that appears in Fig 2 A. **B: Heatmap Tables of Absolute Differences in Synaptic Distribution**: Illustration of heatmap tables of the absolute differences in synaptic distributions. On the left, the difference is between a synaptic distribution based on literature review and one predicted by the Genetic Algorithm. On the right, the difference is between a synaptic distribution based on literature review and a completely random distribution. Each row corresponds to a particular pair of connections. Columns L1 to L6 represent the six different layers of the cortex. The intensity of the color in each cell represents the magnitude of the difference, with a darker shade of red indicating a larger difference.

An additional observation arising from the experimental conditions relates to cortical layers 2 and 3. Typically, experimental procedures do not differentiate between these two layers, treating them as a single layer (2/3). Adopting this approach in our synaptic distribution table could potentially enhance the alignment between the data from literature (Table I) and the distribution predicted by the Genetic Algorithm (Fig. 7B), especially in the case of the second pyramidal cell. This hypothesis stems from the consistent pattern observed in both tables: when the probabilities for layers 2 and 3 are summed, the resulting value is always equal to or greater than that for layer 1. Thus, considering layers 2 and 3 as a unified entity could potentially refine our understanding and modeling of the synaptic distribution.

Further comparison of these two different synaptic distributions can be found in Table III, which calculates the cross-correlation between the one predicted by the GA and the literature-derived distribution, as well as between the random distribution and the literature data. In this analysis, higher cross-correlation values nearing 1 indicate a higher degree of similarity between datasets, while values approaching -1 suggest greater divergence.

The 'Literature vs. Random' column reveals that the cross-correlation values for most synaptic connections predominantly fall within a range of 0.22 to 0.37, except for 'ext→P2', which registers a considerably lower value of 0.05. This suggests that, aside from 'ext→P2', the random distribution generally exhibits some level of correlation with the literature-based dataset.

Moving on to the 'Literature vs. Predicted' column, most synaptic connections' values are comparable to or

TABLE III. Cross-correlation between the distribution of the synapses computed from literature and a random distribution (Lit. vs. Random), and between the one from literature and the predicted by the genetic algorithm (Lit. vs. Predicted).

Synapses	Lit. vs. Random	Lit. vs. Predicted
ext→P1	0.23	0.21
SS→P1	0.22	0.20
SST→P1	0.24	0.20
P2→P1	0.28	0.29
P2→P2	0.37	0.33
PV→P2	0.35	0.20
ext→P2	0.05	0.34
P1→P2	0.31	0.32

slightly lower than those in the random distribution. Interestingly, the 'ext→P2' correlation shows a marked improvement to 0.34, in contrast to its random counterpart at 0.05, indicating a stronger alignment with the literature data in the GA prediction.

To summarize, these findings imply that, while the GA-predicted distribution exhibits a degree of alignment with the literature data, in most cases, the random distribution shows a slightly higher correlation. This observation warrants further investigation and refinement of the predictive model to enhance its ability to emulate experimental data and maintain physiological relevance.

IV. DISCUSSION

This study aimed to enhance the precision of the laminar Neural Mass Model (LaNMM) to better simulate the observed neuronal behavior in experimental data. Our work is motivated by the increasing recognition of gamma oscillations' pivotal role in various cognitive functions and their association with several neurological and psychiatric disorders, particularly Alzheimer's disease [1]. The ongoing advances in non-invasive brain stimulation techniques, like 40 Hz transcranial alternating current stimulation (tACS), underscore the need for more accurate and physiologically relevant models [3, 4]. In this context, the LaNMM integrates two well-established models—Jansen and PING—to induce slow and fast oscillations within the alpha and gamma frequency bands, respectively [11]. In order to refine this model, we physically embedded it within a multi-compartmental neuron model, which allows us to compare the model's predictions directly against experimental data [13].

Our first significant modification involved adjusting the external input noise in the model, representing largely inputs originating from the thalamus and other cortical regions. We found that altering the standard deviation of this noise is crucial for aligning the model with experimental data. After conducting a thorough study on various values, we set it at 200 Hz.

With respect to the dual-frequency approach, it is evident that the LaNMM's predictions match well with the experimental data. Moreover, the model's intrinsic capacity to produce dominant alpha and gamma frequencies was robustly observed, even when we used a random synaptic distribution. However, the results obtained assuming a random synaptic distribution significantly deviated from the experimental data when evaluating the relative power distribution across cortical depth, especially within the gamma frequency band. This discrepancy highlights the need for refining our model with a more informed synaptic distribution.

In response to these findings, we employed a Genetic Algorithm (GA) to optimize our model. Our aim was to align the distribution of the model-simulated relative power more closely with the experimental data. Despite occasional stagnation due to local minima, the GA proved to be an efficient tool in refining the synaptic distribution. We achieved a Pearson coefficient of 0.67—an impressively high value considering the context of experimental data. The results clearly show that the relative powers with the predicted synaptic distribution closely resemble the experimental data compared to simulations using a random distribution of synapses.

In our final analysis, we compared both the GA-based predictions and a random distribution with the literature-based distribution, in order to assess biological validity. While the random distribution often aligns slightly better with the literature data, the GA-predicted distribution demonstrates smoother transitions and superior alignment for specific connections, such as 'ext→P2'. Nevertheless, certain discrepancies, notably in the PV→P2 connection, indicate areas for further refinement.

Overall, our comparisons of synaptic distributions have shed light on the complexity of cortical layer interactions. Although the random distribution generally exhibits a higher correlation with the literature, the GA-predicted distribution's smooth transitions and alignment in specific connections revealed its potential for greater accuracy. These findings underscore the need for continuous model refinement to better replicate experimental data and maintain physiological relevance.

V. LIMITATIONS OF THE STUDY AND CONCLUSIONS

Our study makes significant contributions to understanding the potential of Neural Mass Models for simulating physiological data, but it is also subject to certain limitations.

Firstly, our research is constrained by assumptions about the architecture of the two pyramidal cells involved in the laminar model. We hypothesize that the first cell spans from layer 1 to layer 5, while the second extends from layer 1 to layer 3. Future research should aim to explore different configurations of these pyramidal cells

and examine how changes in their architecture influence the model's predictions.

Secondly, we derived the synapse distribution utilized in our study for validation from existing literature. However, the current understanding of synapse distribution is still evolving, and the complexity of the required experiments means that data is limited. Most notably, the distinction between layers 2 and 3 is often omitted in the existing literature; we chose to include this separation to better compare our predicted synapse distribution. A more refined understanding of synapse distribution across different layers, provided by future research, would significantly enhance our ability to validate our model's predictions.

Thirdly, the application of our model was limited to experimental data from a single subject. To strengthen the robustness and applicability of our findings, it would be beneficial for future studies to incorporate data from multiple subjects. This would not only ensure the validity of the model's predictions across different individuals but could also highlight potential variations in synaptic distribution.

Lastly, given our use of a genetic algorithm in this study, there is an opportunity for future research to explore larger simulations. This could lead to an increased correlation between simulated and experimental data, potentially improving the predictive precision of the model.

Despite certain limitations, our study highlights the utility of Neural Mass Models as powerful tools for unraveling the complexities of the brain. Our research paves the way for a deeper understanding of neurological disorders and establishes a strong foundation for developing a model that accurately predicts the effects of transcranial Alternating Current Stimulation (tACS). Future work will build upon these findings, utilizing this refined model to analyze the remaining data and investigate the neural responses before and after tACS, bringing us one step closer to devising more effective treatments and interventions for a range of neurological conditions.

APPENDIX

Pseudocode of the Genetic Algorithm

In this section, we present a simplified pseudocode of the Genetic Algorithm that we created for this study. The algorithm aims to optimize a synaptic distribution used in the physically embedded laminar Neural Mass Model to achieve a more accurate replication of experimental data.

The variables used in the pseudocode are as follows:

- P: Population
- ρ_{alpha}: Pearson coefficient for the alpha band
- ρ_{gamma}: Pearson coefficient for the gamma band
- ρ: Total Pearson coefficient
- P_{size}: Population size
- N_{gen}: Number of generations
- r_m: Mutation rate
- r_c: Crossover rate
- $\overline{S}^{NIexp}$: Non-interpolated relative powers obtained by experimental data
- $\overline{S}^{exp}$: Interpolated relative powers obtained by experimental data
- $\overline{S}_\alpha$: Simulated relative powers for the alpha band
- $\overline{S}_\gamma$: Simulated relative powers for the gamma band
- Par: Parent
- Off: Offspring
- c: Chromosome
- ν: Distribution of synapses matrix
- T: Total power spectra
- ω: Frequency

Algorithm 1 Genetic Algorithm for Optimizing a Synaptic Distribution

```
P ← InitializePopulation
ρ_α, ρ_γ, ρ ← 0
ρ_α_list, ρ_γ_list, ρ_list ← [ ]
procedure GA(S̄^NIexp, P_size, N_gen, r_m, r_c)
    S̄^exp ← Interpolate(S̄^NIexp)
    for i ∈ range(N_gen) do
        for c ∈ P do
            ρ_α, ρ_γ, ρ ← Fitness(c, S̄^exp)
            ρ_α_list ← Add(ρ_α_list, ρ_α)
            ρ_γ_list ← Add(ρ_γ_list, ρ_γ)
            ρ_list ← Add(ρ_list, ρ)
        end for
        if max(ρ_list) > BestFit then
            BestFit ← max(ρ_list)
            BestSol ← P[argmax(ρ_list)]
        end if
        if max(ρ_α_list) > BestFit_α then
            BestFit_α ← max(ρ_α_list)
        end if
        if max(ρ_γ_list) > BestFit_γ then
            BestFit_γ ← max(ρ_α_list)
        end if
        for j ∈ range(P//2) do
            Par1, Par2 ← Selection(P, ρ_list)
            Off1, Off2 ← InterCros(Par1, Par2, r_c)
            Off1, Off2 ← Mutation(Off1, Off2, r_m)
            NewP ← Add(NewP, Off1, Off2)
        end for
        P ← NewP
    end for
    return BestSol, BestFit, BestFit_α, BestFit_γ
end procedure
```

procedure FITNESS(c, $\overline{S}^{exp}$)
  $\overline{S}_\alpha, \overline{S}_\gamma \leftarrow$ COMPRELP($cortex, node\_id, \nu, fs, nsec$)
  $\rho_\alpha \leftarrow$ PEARSONR($\overline{S}^{exp}, \overline{S}_\alpha$)
  $\rho_\gamma \leftarrow$ PEARSONR($\overline{S}^{exp}, \overline{S}_\gamma$)
  $\rho \leftarrow (\rho_\alpha + \rho_\gamma)/2$
  return $\rho_\alpha, \rho_\gamma, \rho$
end procedure

procedure SELECTION(P, ρ_list)
  for $c \in P$ **do**
    $SelProb\_list \leftarrow$ PROB. BASED ON $\rho\_list[c]$
  end for
  $Parent1, Parent2 \leftarrow$ BASED ON $SelProb\_list$
  return $Parent1, Parent2$
end procedure

procedure INTERCROS($Par1$, $Par2$, r_c)
  if RAND_NUM $< r_c$ **then**
    $W \leftarrow$ RANDOM_MATRIX
    for $i \in$ RANGE($Par1\_size[0]$) **do**
      $Off1[i,:] \leftarrow W[i] \cdot Par1[i,:] + (1 - W[i]) \cdot Par2[i,:]$
      $Off2[i,:] \leftarrow W[i] \cdot Par2[i,:] + (1 - W[i]) \cdot Par1[i,:]$
      $Off1\_norm[i,:] \leftarrow$ NORMALIZE($Off1[i,:]$)
      $Off2\_norm[i,:] \leftarrow$ NORMALIZE($Off2[i,:]$)
    end for
    return $Off1\_norm, Off2\_norm$
  else
    return $Par1, Par2$
  end if
end procedure

procedure MUTATION(c, r_m)
  if RAND NUM $< r_m$ **then**
    $i, j \leftarrow$ SELECT INDEX RANDOMLY
    $c\_new \leftarrow$ MUTATE($c_{i,j}$)
    $c\_norm \leftarrow$ NORMALIZE($c[i,:]$)
  end if
  return c_norm
end procedure

procedure COMPRELP($cortex, node\_id, \nu, fs, nsec$)
  $NMM \leftarrow$ CORTICALPATCH($cortex, node\_id, \nu$)
  $CSD \leftarrow$ TRANSLATE NMM TO CSD
  $Voltage \leftarrow$ CALCULATE VOLTAGE FROM CSD
  $bLFP \leftarrow$ np.diff($Voltage$)
  $\overline{S} \leftarrow$ WELCH($bLFP, fs, nsec$)
  $T \leftarrow$ np.sum($\overline{S}$)
  $\omega_\alpha, \omega_\gamma \leftarrow \alpha : [4, 22], \gamma : [32, 48]$
  $\overline{S}_\alpha \leftarrow$ np.sum($\overline{S}(\omega)/T), \omega \in \omega_\alpha$
  $\overline{S}_\gamma \leftarrow$ np.sum($\overline{S}(\omega)/T), \omega \in \omega_\gamma$
  return $\overline{S}_\alpha, \overline{S}_\gamma$
end procedure

ACKNOWLEDGMENTS

I am profoundly grateful for the support and guidance I received throughout my Master's thesis journey.

First, my deepest appreciation goes to my supervisors. To Pau Clusella, for his ceaseless mentorship, insightful guidance, and wisdom, which all made this endeavor both stimulating and fulfilling. His expertise has been instrumental, and I have learned tremendously under his tutelage. To Roser Sánchez-Todo, who, with her infectious cheerfulness, made me feel an integral part of the Neuroelectrics team. Her assistance in understanding her work became a cornerstone of this thesis. And to Jordi Soriano, for his advice, steadfast support, and inspirational passion for neuroscience that have been a guiding beacon for me over the years and throughout this thesis.

I also wish to express my sincere gratitude to the Neuroelectrics team. Special thanks go to Guilio Ruffini for giving me the opportunity to contribute to this project, and to Borja Mercadal, whose help in understanding and incorporating his work into this study was indispensable.

My appreciation extends to the UPO team for their help with the biological aspects of this thesis, and to everyone who participated in the Neurotwin project. Their collective efforts not only made this study possible but are also contributing significantly to the advancement of science. Being a part of this project has been a privilege.

Finally, I wish to express my deepest gratitude to Pol for his unwavering support, patience, and belief in me. My friends have also been a pillar of support and understanding, and their encouragement has meant the world to me. To my family, your support, faith, and positivity have been my strength throughout this journey.

Thank you all for your significant contributions that have profoundly shaped this work. The privilege of learning from such brilliant minds and being a part of this incredible community has been immeasurable.

[1] J. J. Palop and L. Mucke, "Network abnormalities and interneuron dysfunction in alzheimer disease," *Nature Reviews Neuroscience*, vol. 17, no. 12, pp. 777–792, 2016. [Online]. Available: https://doi.org/10.1038/nrn.2016.141

[2] A. Traikapi and N. Konstantinou, "Gamma oscillations in Alzheimer's disease and their potential therapeutic role," *Frontiers in systems neuroscience*, vol. 15, p. 782399, 2021. [Online]. Available: https://doi.org/10.3389/fnsys.2021.782399

[3] G. Sprugnoli, F. Munsch, D. Cappon, R. Paciorek, J. Macone, A. Connor, G. El Fakhri, R. Salvador, G. Ruffini, K. Donohoe, M. M. Shafi, D. Press, D. C. Alsop, A. Pascual Leone, and E. Santarnecchi, "Impact of multisession 40hz tacs on hippocampal perfusion in patients with alzheimer's disease," *Alzheimer's research & therapy*, vol. 13, no. 1, p. 203, 2021. [Online]. Available: ClinicalTrials.gov/NCT03412604, ClinicalTrials.gov/NCT03290326

[4] S. Grover, W. Wen, V. Viswanathan, C. T. Gill, and R. M. G. Reinhart, "Long-lasting, dissociable improvements in working memory and long-term memory in older adults with repetitive neuromodulation," *Nature Neuroscience*, vol. 25, no. 9, pp. 1237–1246,

2022. [Online]. Available: https://doi.org/10.1038/s41593-022-01132-3

[5] A. Antal and W. Paulus, "Transcranial alternating current stimulation (tacs)," *Frontiers in Human Neuroscience*, vol. 7, p. 317, 2013. [Online]. Available: https://www.frontiersin.org/articles/10.3389/fnhum.2013.00317/full

[6] H. R. Wilson and J. D. Cowan, "Excitatory and inhibitory interactions in localized populations of model neurons," *Biophysical journal*, vol. 12, no. 1, pp. 1–24, Jan 1972. [Online]. Available: https://doi.org/10.1016/S0006-3495(72)86068-5

[7] W. J. Freeman, "Linear analysis of the dynamics of neural masses," *Annual Review of Biophysics and Bioengineering*, vol. 1, no. 1, pp. 225–256, 1972, pMID: 4346305. [Online]. Available: https://doi.org/10.1146/annurev.bb.01.060172.001301

[8] ——, *Mass Action in the Nervous System*. New York: Academic Press, 1975.

[9] F. H. Lopes da Silva, A. Hoeks, H. Smits, and L. H. Zetterberg, "Model of brain rhythmic activity. the alpha-rhythm of the thalamus," *Kybernetik*, vol. 15, no. 1, pp. 27–37, May 1974. [Online]. Available: https://doi.org/10.1007/BF00270757

[10] F. Grimbert and O. Faugeras, "Analysis of jansen's model of a single cortical column," Inria, Research Report RR-5597, 2006. [Online]. Available: https://hal.inria.fr/inria-00070410/file/RR-5597.pdf

[11] R. Sanchez-Todo, A. M. Bastos, E. Lopez-Sola, Mercadal, E. Santarnecchi, E. K. Miller, G. Deco, and G. Ruffini, "A physical neural mass model framework for the analysis of oscillatory generators from laminar electrophysiological recordings," *NeuroImage*, vol. 270, p. 119938, 2023. [Online]. Available: https://www.sciencedirect.com/science/article/pii/S105381192300085X

[12] J. F. Mejias, J. D. Murray, H. Kennedy, and X.-J. Wang, "Feedforward and feedback frequency-dependent interactions in a large-scale laminar network of the primate cortex," *Science advances*, vol. 2, no. 11, p. e1601335, Nov 2016. [Online]. Available: https://doi.org/10.1126/sciadv.1601335

[13] B. Mercadal, E. Lopez-Sola, A. Galan-Gadea, M. Al Harrach, R. Sanchez-Todo, R. Salvador, F. Bartolomei, F. Wendling, and G. Ruffini, "Towards a mesoscale physical modeling framework for stereotactic-eeg recordings," *Journal of Neural Engineering*, vol. 20, no. 1, 2023. [Online]. Available: https://doi.org/10.1088/1741-2552/acae0c

[14] Neuroelectrics Barcelona SLU, "Software design document bm-swd0005," 2021, unpublished internal company document.

[15] Starlab SL, "NeuroTwin," https://www.neurotwin.eu/, accessed: Apr. 5, 2023.

[16] G. Buzsáki, C. A. Anastassiou, and C. Koch, "The origin of extracellular fields and currents — EEG, ECoG, LFP and spikes," *Nature Reviews Neuroscience*, vol. 13, no. 6, pp. 407–420, Jun. 2012. [Online]. Available: https://doi.org/10.1038/nrn3241

[17] J. J. Jun, N. A. Steinmetz, J. H. Siegle, D. J. Denman, M. Bauza, B. Barbarits, A. K. Lee, C. A. Anastassiou, A. Andrei, Aydın, M. Barbic, T. J. Blanche, V. Bonin, J. Couto, B. Dutta, S. L. Gratiy, D. A. Gutnisky, M. Häusser, B. Karsh, P. Ledochowitsch, C. M. Lopez, C. Mitelut, S. Musa, M. Okun, M. Pachitariu, J. Putzeys, P. D. Rich, C. Rossant, W.-l. Sun, K. Svoboda, M. Carandini, K. D. Harris, C. Koch, J. O'Keefe, and T. D. Harris, "Fully integrated silicon probes for high-density recording of neural activity," *Nature*, vol. 551, no. 7679, pp. 232–236, 11 2017. [Online]. Available: https://doi.org/10.1038/nature24636

[18] P. Clusella and M. Moreno, "Modeling and analysis of tacs stimulation in mice cortex multilayer recordings," unpublished slides presented at the Neurotwin 5th Plenary Meeting, Seville, March 2023.

[19] G. Buzsáki, C. A. Anastassiou, and C. Koch, "The origin of extracellular fields and currents — eeg, ecog, lfp and spikes," *Nature Reviews Neuroscience*, vol. 13, no. 6, pp. 407–420, 2012. [Online]. Available: https://doi.org/10.1038/nrn3241

[20] D. B. Percival and A. T. Walden, *Spectral Analysis for Physical Applications*, 1st ed. Cambridge University Press, Jun. 1993. [Online]. Available: http://doi.org/10.1017/CBO9780511622762

[21] F. Lopes da Silva, A. van Rotterdam, P. Barts, E. van Heusden, and W. Burr, "Models of neuronal populations: The basic mechanisms of rhythmicity," in *Perspectives in Brain Research*, ser. Progress in Brain Research, M. Corner and D. Swaab, Eds. Elsevier, 1976, vol. 45, pp. 281–308. [Online]. Available: https://www.sciencedirect.com/science/article/pii/S0079612308609954

[22] A. M. Bastos, R. Loonis, S. Kornblith, M. Lundqvist, and E. K. Miller, "Laminar recordings in frontal cortex suggest distinct layers for maintenance and control of working memory," *Proceedings of the National Academy of Sciences*, vol. 115, no. 5, pp. 1117–1122, 2018. [Online]. Available: https://www.pnas.org/doi/abs/10.1073/pnas.1710323115

[23] C. Börgers, S. Epstein, and N. J. Kopell, "Gamma oscillations mediate stimulus competition and attentional selection in a cortical network model," *Proceedings of the National Academy of Sciences*, vol. 105, no. 46, pp. 18 023–18 028, 2008. [Online]. Available: https://www.pnas.org/doi/abs/10.1073/pnas.0809511105

[24] B. Molaee-Ardekani, P. Benquet, F. Bartolomei, and F. Wendling, "Computational modeling of high-frequency oscillations at the onset of neocortical partial seizures: From 'altered structure' to 'dysfunction'," *NeuroImage*, vol. 52, no. 3, pp. 1109–1122, 2010, computational Models of the Brain. [Online]. Available: https://www.sciencedirect.com/science/article/pii/S105381190901338X

[25] C. Quairiaux, P. Mégevand, J. Z. Kiss, and C. M. Michel, "Functional development of large-scale sensorimotor cortical networks in the brain," *The Journal of Neuroscience*, vol. 31, no. 26, pp. 9574–9584, 2011. [Online]. Available: https://doi.org/10.1523/JNEUROSCI.5995-10.2011

[26] E. R. Kandel, J. D. Koester, S. H. Mack, and S. A. Siegelbaum, *Notice*. New York, NY: McGraw Hill, 2021. [Online]. Available: neurology.mhmedical.com/content.aspx?aid=1180370227

[27] D. Feldmeyer, G. Qi, V. Emmenegger, and J. F. Staiger, "Inhibitory interneurons and their circuit motifs in the many layers of the barrel cortex," *Neuroscience*, vol. 368, pp. 132–151, 2018, barrel Cortex Function. [Online]. Available: https://www.sciencedirect.com/science/article/pii/S0306452217303524

[28] D. H. Hubel, "Exploration of the primary visual cortex, 1955–78," *Nature*, vol. 299, no. 5883, pp. 515–524, 1982. [Online]. Available: https://doi.org/10.1038/299515a0

[29] R. J. Douglas and K. A. C. Martin, "Neuronal circuits of the neocortex," *Annual Review of Neuroscience*, vol. 27, pp. 419–451, 2004. [Online]. Available: https://doi.org/10.1146/annurev.neuro.27.070203.144152

[30] Z. Almási, C. Dávid, M. Witte, and J. F. Staiger, "Distribution patterns of three molecularly defined classes of gabaergic neurons across columnar compartments in mouse barrel cortex," *Frontiers in Neuroanatomy*, vol. 13, p. 45, 2019. [Online]. Available: https://doi.org/10.3389/fnana.2019.00045

[31] K. D. Harris and T. D. Mrsic-Flogel, "Cortical connectivity and sensory coding," *Nature*, vol. 503, no. 7474, pp. 51–58, 2013. [Online]. Available: https://doi.org/10.1038/nature12654

[32] S. L. Hill, Y. Wang, I. Riachi, F. Schürmann, and H. Markram, "Statistical connectivity provides a sufficient foundation for specific functional connectivity in neocortical neural microcircuits," *Proceedings of the National Academy of Sciences*, vol. 109, no. 42, pp. E2885–E2894, 2012. [Online]. Available: https://www.pnas.org/doi/abs/10.1073/pnas.1202128109

[33] S. Luke, *Essentials of Metaheuristics*, 2nd ed. Lulu, 2013. [Online]. Available: http://cs.gmu.edu/$\sim$sean/book/metaheuristics/

[34] A. Hassanat, K. Almohammadi, E. Alkafaween, E. Abunawas, A. Hammouri, and V. B. S. Prasath, "Choosing mutation and crossover ratios for genetic algorithms—a review with a new dynamic approach," *Information*, vol. 10, no. 12, 2019. [Online]. Available: https://www.mdpi.com/2078-2489/10/12/390